P- AND S-WAVE SEPARATION AND DECOMPOSITION OF TWO- AND THREE-COMPONENT ELASTIC SEISMOGRAMS

WENLONG WANG[1] and GEORGE A. MCMECHAN[2]

[1] *Department of Mathematics, Harbin Institute of Technology, 92 Xidazhi St., Nangang Dist., Harbin, Heilongjiang 150001, P.R. China. wenlong.wang@hit.edu.cn*
[2] *Center for Lithospheric Studies, The University of Texas at Dallas, 800 W. Campbell Road, Richardson, TX 75080-3021, U.S.A. mcmec@utdallas.edu*

(Received April 15, 2019; accepted July 24, 2019)

ABSTRACT

Wang, W. and McMechan, G.A., 2019. P- and S-wave separation and decomposition of two- and three-component elastic seismograms. *Journal of Seismic Exploration*, 28: 425-447.

Multi-component seismic data are valuable in estimating subsurface elastic parameters. The coexistence of P- and S-waves in multi-component surface seismic data poses an obstacle in extracting the elastic properties. Thus, it is crucial to separate the P- and S-waves in elastic seismograms, or during wavefield extrapolations. We analyze an algorithm that can perform both P- and S-wave separation and vector decomposition of multi-component elastic seismograms that are collected from various media, including isotropie, heterogeneous and transversely isotropie, and we extend it to 3D. This algorithm is based on the dispersion relations of P- and S-waves in isotropic and anisotropic wavefields; the near-surface velocity zone can be separated into several segments horizontally to handle heterogeneity. The algorithm is efficient, and no elastic wavefield extrapolations are needed to perform the separation or decomposition, so no subsurface information is needed, apart from the near-surface model parameters (i.e., P- and S-wave velocities, anisotropic parameters) along the receiver arrays. Tests with synthetic data from various 2D and 3D models show high accuracy by comparing the separation and decomposition results from benchmarks that can only be obtained during elastic wavefield forward modeling.

KEY WORDS: elastic, seismogram, separation, decomposition, 3D.

0963-0651/19/$5.00

INTRODUCTION

P- and S-waves provide independent information on subsurface properties. Joint analysis of P- and S-waves demonstrates benefits in detecting fluids, gas clouds, fracturing, and anisotropy (Zhu et al., 1999). However, the P- and S-waves are coupled, and they need to be separated either in the recorded seismograms or during wavefield extrapolations to provide separate P- and S-wave images. In this paper, we focus on separating multi-component surface seismograms into their P- and S-wave components.

P- and S-wave separation in seismograms has been investigated for decades. Dankbaar (1985) applies a filter in the wavenumber-frequency domain to separate the P- and S-waves and to remove the response of the receiver array, in which the filter coefficients are determined from the near-surface P- and S-wave velocities and geophone geometries. Devaney and Oristaglio (1986) separate 2D elastic vertical seismic profile (VSP) data into P- and S-waves with a plane-wave decomposition. Greenhalgh et al. (1990) apply a dot-product between the particle motion vector and the slowness vector to separate the P- and S-waves in the τ-p domain. Amundsen (1995) derives an algorithm from boundary conditions at the seafloor to separate the multi-component data into upgoing and downgoing P- and S-waves. Sun (1999) separates the 2D elastic seismograms by a sequential procedure of a downward elastic extrapolation, application of the divergence and curl operators, followed by an upward acoustic extrapolation. Wang et al. (2002) applies the P- and S-wave (PS) separation in the τ-p domain with the amplitudes preserved. van der Baan (2006) adapts independent- component analysis for separation. Li et al. (2015), Wang et al. (2015), and Wang et al. (2016) followed a similar procedure to decompose multi-component seismogram into P- and S-wave parts while preserving the vector components by doing elastic extrapolations with decoupled elastic equations. Stanton and Sacchi (2017) incorporate PS decomposition in elastic one-way extrapolations. Wang and Cheng (2017) separate multi-component seismograms in anisotropic media with low-rank approximations.

In this paper, we investigate an algorithm that is based on dispersion relations, and can perform a PS separation and give results similar to those of the divergence and curl operators, or perform a PS decomposition which preserves the vector components of the P- and S-waves. The dispersion relation has been used in separating P-and S-waves (Devaney and Oristaglio, 1986; Wapenaar et al., 1990). The methodology is applied to VSP data by Yao et al. (1993). Li et al. (2016) present a similar approach, implemented only for 2D isotropic media. In this paper, we generalize this decomposition to include transverse isotropy, and extend it to 3D. We also investigate a different procedure to handle lateral heterogeneity at the near-surface, which generates reliable results. The results are analyzed and benchmarked with results that are directly obtained during synthetic forward modeling with PS separation/decomposition schemes embedded.

The paper is organized as follows. First, the concepts and methodologies for multi-component seismogram PS separation and decomposition are introduced. Then, four tests using synthetic data generated from a 2D isotropic model, a transversely isotropic model with a vertical symmetry axis (VTI), a heterogeneous model, and a 3D isotropic model, respectively, are performed to illustrate and to evaluate the quality of the PS separation and decomposition.

METHODOLOGY

There are two categories of algorithms that separate wavefields and seismograms into P- and S-wave parts (Zhang and McMechan, 2010). One is "PS separation", here represented by divergence and curl (or similar) operators, which does not preserve amplitude and phase; the other is "PS decomposition", which uses the relations between wave propagation and polarization vectors, and does preserve amplitude and phase.

In PS separation of isotropic wavefields, the resultant P-waves are scalars

$$\Phi = \nabla \cdot \mathbf{U}, \tag{1}$$

while the resultant S-waves are vectors (in 2D, there is only one non-zero S-wave vector component)

$$\mathbf{\Psi} = \nabla \times \mathbf{U}, \tag{2}$$

where $\mathbf{U}$ is the coupled elastic particle-velocity wavefield snapshot, and Φ and $\mathbf{\Psi}$ are the separated P- and S-waves, respectively. Equivalent expressions in the wavenumber domain are

$$\tilde{\Phi} = i\mathbf{k} \cdot \tilde{\mathbf{U}}, \tag{3}$$

and

$$\tilde{\mathbf{\Psi}} = i\mathbf{k} \times \tilde{\mathbf{U}}, \tag{4}$$

where a tilde over the wavefield indicates a Fourier transform to the wavenumber domain. $\mathbf{k} = (k_x,\ k_y,\ k_z)$ is the wavenumber vector, and i is the imaginary unit.

The amplitude and phase of the separation results using eqs. (1) - (4) are changed relative to those of the input (Sun, 1999), and so their recovery needs extra work (Sun et al., 2001). To avoid this problem, the PS decomposition is proposed (Ma and Zhu, 2003; Zhang et al., 2007; Zhang and McMechan, 2010; Wang et al., 2015; Zhu, 2017), which aims at separating the wavefield $\mathbf{U}$ while preserving the corresponding P and S particle-velocity components

$$\mathbf{U} = \mathbf{U}^P + \mathbf{U}^S, \tag{5}$$

where the coupled vector wavefield $\mathbf{U}$ is decomposed into P ($\mathbf{U}^P$) and S ($\mathbf{U}^S$) waves, respectively. The P-waves are decomposed in the wavenumber domain (Zhang and McMechan, 2010) using

$$\widetilde{\mathbf{U}}^P = \mathbf{A}^P(\mathbf{A}^P \cdot \widetilde{\mathbf{U}}), \tag{6}$$

where $\mathbf{A}^P$ is the normalized P-wave polarization direction, which is equivalent to a normalized wavenumber vector in isotropic media, or can be obtained by solving the Christoffel equation in the wavenumber domain for anisotropic media (Dellinger and Etgen, 1990). $\widetilde{\mathbf{U}}^P$ contains the decomposed P-waves in the wavenumber domain, and can be transformed back to the space domain by inverse FFTs. The S-waves $\mathbf{U}^S$ can be calculated either by eq. (18) in Zhang and McMechan (2010), or by a component-by-component subtraction of the P-waves from the original coupled wavefield $\mathbf{U}$ using eq. (5).

Both the separation and the decomposition algorithms can be implemented in the wavenumber domain; the divergence and curl operators can also be applied in the space domain with increased efficiency. However, a multi-component seismogram dataset recorded along the surface does not have the vertical or k_z dimension, so eqs. (1) - (4) and (5) - (6) cannot be applied directly. In isotropoic media with a homogeneous surface, the propagations of P- and S-waves satisfy the dispersion relation

$$q_z^m = -\sqrt{\frac{1}{[V^m]^2} - q_x^2 - q_y^2}, \tag{7}$$

where the superscript m stands for the wave mode (P or S); $q_i = k_i/\omega$ stands for the slowness in the direction i ($i = x$, y or z); and ω is the angular frequency. One assumption is that the recorded waves are all up-going, which means that the vertical slowness is negative. A normalized P-wave slowness vector can be used as the polarization direction in eq. (6).

In VTI media, the dispersion relation is more complicated, but a vertical slowness q_z of each wave mode can be expressed in a form similar to eq. (7) with assumptions (Schoenberg and de Hoop, 2000; Pedersen et al., 2007). It also requires parameters, other than wave velocities, to be involved in the calculation [i.e., ϵ and δ in weak anisotropy (Thomsen, 1986)]. Note that an anisotropic dispersion relation is required only if the near-surface model is anisotropic. If the subsurface is VTI or another type of anisotropy, but the model parameters along the receivers are isotropic, then the isotropic dispersion relation in eq. (7) still applies.

To handle velocity heterogeneity along the receiver arrays in isotropic models, the near-surface velocity zone can be separated into multiple

horizontal sections, and the P- and S-wave velocities vary smoothly within each section. Then the dispersion relation can be calculated separately within each section, and V^m in eq. (7) becomes the averaged velocity of the wave mode m in each section.

One problem in separating the P- and S-waves using divergence and curl operators is that the amplitudes and phases are changed after the separation. This is caused by the spatial derivative operators in eqs. (1) and (2), or the multiplications of the wavefields with ik_x, ik_y and ik_z in eqs. (3) and (4). A solution to avoid the amplitude change is to use a normalized slowness vector

$$Q_i^m = q_i/\sqrt{q_x^2 + q_y^2 + (q_z^m)^2}, \tag{8}$$

where the capital letter Q represents the normalized wavenumber with the subscript $i = x, y, z$. Eq. (8) gives the normalized slowness vectors $\boldsymbol{Q}$ which satisfies the dispersion relations of the P- and the S-waves, respectively. Regarding the fact that the P-wave is curl-free since all displacements are in the direction of wave motion and the fact that the S-wave is divergence-free since displacements are orthogonal to wave motion (Morse and Feshbach, 1953), the equations

$$\mathbf{Q}^P \times \tilde{\mathbf{U}}^P = \mathbf{0}, \tag{9}$$

and

$$\mathbf{Q}^S \cdot \tilde{\mathbf{U}}^S = 0, \tag{10}$$

are valid. Thus, the P-waves can be separated as

$$\tilde{\Phi}' = i\mathbf{Q}^S \cdot \tilde{\mathbf{U}}^P = i\mathbf{Q}^S \cdot \tilde{\mathbf{U}}, \tag{11}$$

and the S-waves as

$$\tilde{\boldsymbol{\Psi}}' = i\mathbf{Q}^P \times \tilde{\mathbf{U}}^S = i\mathbf{Q}^P \times \tilde{\mathbf{U}}, \tag{12}$$

Comparing with eqs. (3) and (4), the unnormalized wavenumber vector $\mathbf{k}$ is substituted by $\mathbf{Q}^P$ and $\mathbf{Q}^S$, which are normalized in eqs. (11) and (12). Thus, the amplitudes of the separated P ($\tilde{\Phi}'$) and S ($\tilde{\boldsymbol{\Psi}}'$) waves in the separation algorithm are preserved and correct. The phases are still shifted by 90°, and can be corrected using Hilbert transforms (Sun et al., 2001), but the phase corrections are not performed in the following synthetic-tests section to facilitate comparisons with the divergence and curl methods.

Similarly, the multi-component P-wave seismogram can be obtained by decomposition as

$$\tilde{\mathbf{U}}^P = \mathbf{Q}^P(\mathbf{Q}^S \cdot \tilde{\mathbf{U}}), \tag{13}$$

where the dot product $\mathbf{Q}^S \cdot \tilde{\mathbf{U}}$ removes the S-waves from the seismogram, and the multiplication by $\mathbf{Q}^P$ restores the vector components of the P-waves.

The procedures for performing PS separation and vector decomposition are very similar, and thus are combined within the same framework. The separation/decomposition of a 3-component seismogram can be summarized as:

1) For each of the x, y, and z particle-velocity components of the input seismogram, perform the 3D Fourier transform from the time-space domain [$\mathrm{U}_x(x,y,t)$, $\mathrm{U}_y(x,y,t)$ and $\mathrm{U}_z(x,y,t)$] to the frequency-wavenumber domain to obtain $\tilde{\mathrm{U}}_x(k_x,k_y,\omega)$, $\tilde{\mathrm{U}}_y(k_x,k_y,\omega)$ and $\tilde{\mathrm{U}}_z(k_x,k_y,\omega)$.

2) If the near-surface zone exhibits significant heterogeneity, then separate the near-surface zone along the receiver array into n sections, within each of which the P- and S-wave velocities vary smoothly. Calculate the average model parameters within each section.

3) Depending on the property of the near-surface model (isotropy or anisotropy), choose a proper dispersion relation to calculate the normalized vectors $\mathbf{Q}^P$ and $\mathbf{Q}^S$.

4) Apply eqs. (11) and (12) for PS separation, or eqs. (13) and (5) for PS vector decomposition.

5) For each component of the separated scalar P-waves and vector S-waves (for PS separation), or each of the x-, y- and z-components of the decomposed P- and/or S-wave (PS decomposition), perform the inverse 3D Fourier transforms from the frequency-wavenumber domain (k_x,k_y,ω) back to the time-space domain (x,y,t).

6) If the near-surface zone is separated into sections to handle heterogeneity, only the separated/decomposed P- and S-seismograms within their corresponding section are harvested as the final results, and repeat step 2 to step 6 for each surface velocity section.

The corresponding procedures for 2-component seismograms are similar except that 2D Fourier transforms are used instead of 3D. Note that for obtaining the S-waves in PS decomposition, the subtraction can be performed in either the time-space or the frequency-wavenumber domain.

SYNTHETIC TESTS

In this section, we apply the separation/decomposition algorithm on synthetic multi-component seismograms, which are generated from 2D models with isotropic homogeneous, anisotropic (VTI) homogeneous, and isotropic heterogeneous near-surface parameters, respectively. Finally, a test

on a 3D isotropic model is performed. For each test on isotropic models, two sets of comparisons are made. We compare the separation and decomposition results with benchmarks that are obtained by divergence and curl operators and decoupled elastic wave equations during extrapolations. PS decomposition is performed on data generated from a VTI model, and the results are compared with those generated by solving for the Christoffel equations. All benchmarks for comparisons can only be obtained during wavefield extrapolation, and have a solid theoretical basis to guarantee correctness (Morse and Feshbach, 1953; Xiao and Leaney, 2010; Zhang and McMechan, 2010).

We use 2D and 3D staggered-grid finite-difference schemes (Virieux, 1986), with second-order accuracy in time, and eighth-order in space, to solve the stress-particle-velocity formulation of the isotropic and anisotropic elastodynamic equations. Absorbing boundary conditions (Komatitsch and Martin, 2007) are used on all grid boundaries (including the top boundary) to reduce unwanted reflections, and are hidden for plotting.

2D flat-layered isotropic model example

The first test is performed on a 2D flat-layered model (Fig. 1), which has 5 m grid spacing in both z- and x-directions. The model parameters from the top layer to the bottom layer are V_P = (2.5, 2.6, 2.7, 2.8) km/s, V_S = (1.4, 1.45, 1.5, 1.55) km/s, and ρ = (2.1, 2.1, 2.1, 2.1) g/cm^3. The P- and S-velocity values in zones along the receiver array are perturbed with a smoothly varying function to simulate velocity heterogeneity. An explosive source with a Ricker time wavelet is placed at (x, z) = (2.0, 0.0) km with dominant frequency of 25 Hz; 801 receivers are evenly spaced along the surface from 0.0 km to 4.0 km. The x- and z-particle velocities are recorded as 2-component seismograms. Fig. 2 contains the 2-component common-source gather with direct waves removed.

We use the PS coupled 2-component seismogram (Fig. 2) as input. We first provide the separation algorithm with averaged near-surface P- and S-wave velocities (V_P = 2.5 km/s, V_S = 1.4 km/s). The separated P- and S-waves are in Figs. 3a and 3b; these can be compared with the results of the divergence and curl operators shown in Figs. 3c and 3d, which can only be obtained during forward modeling. The separation algorithm and the divergence and curl operators give single-component P- and S-waves, because PS separation algorithms generate scalar P-waves and vector S-waves [eqs. (1) – (2)], and in 2D examples, only one non-zero S-wave component remains.

Note that the amplitudes of the P- and S-waves in Figs. 3c and 3d are changed as a result of the divergence and curl operators, and need further corrections to recover the amplitudes. However, the amplitudes in Figs. 3a

and 3b are correct, because the polarization vectors are normalized. The phases of the separated P- and S-waves in both the separation algorithm and the divergence and curl operators are the same, because the former can preserve the amplitude, but not the phase, during separation. The phases of all the separation results in Fig. 3 are all rotated by 90°, which can be corrected by applying Hilbert transforms to all the separated P- and S-waves.

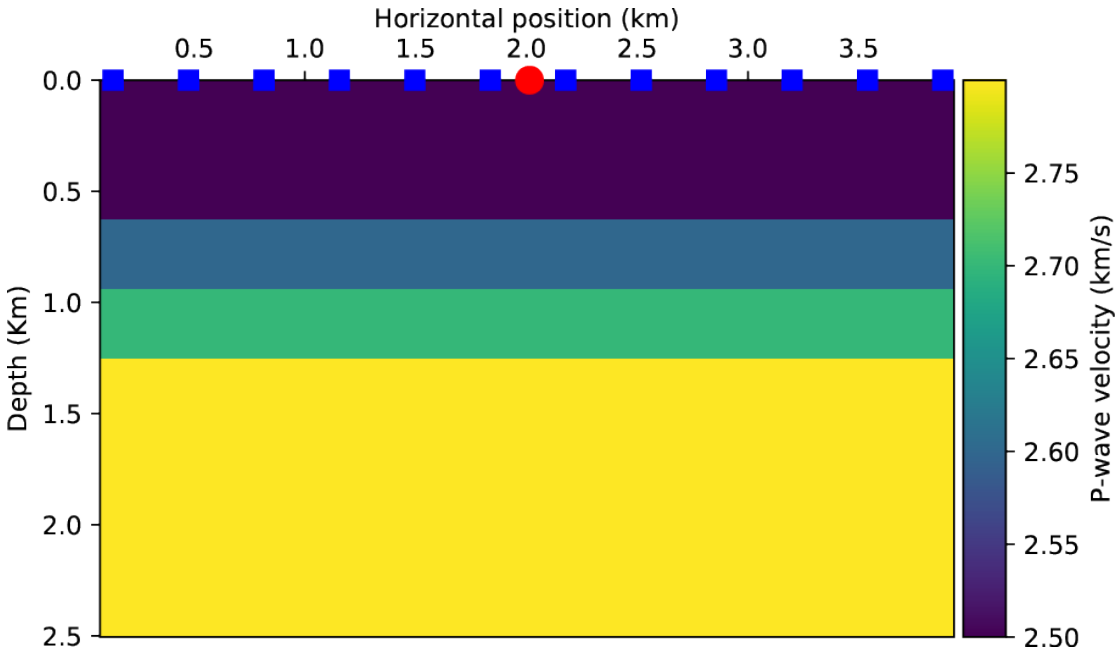

Fig. 1. The flat-layered P-wave velocity model with the source at the red spot, and the blue squares are at every 72nd receiver location. The black boxes indicate the separated velocity zones.

We then apply the decomposition algorithm to the coupled 2-component seismogram (Fig. 2); the resultant decomposed P and S vector seismograms are in Figs. 4a-d. The benchmark decomposed P and S 2-component seismogram using the decoupled equations (Ma and Zhu, 2003; Wang and McMechan, 2015) during the forward modeling are shown in Figs. 4e-h. In both the decomposition algorithm and the decoupled equations, the S-waves are obtained by subtracting the P-wave seismograms from the coupled seismograms component by component, thus the accuracy of the decomposition algorithm can be estimated by subtracting the two sets of P-waves particle-velocity components (Figs. 4a and 4b from Figs. 4e and 4f). The small residuals in Fig. 5 indicate high-quality decomposition results; the largest residuals are 13% of the maximum horizontal P-waves, and 15% of the maximum vertical P-waves. The residuals grow larger as the offset increases, because the reflections are stronger at far offset (AVO effects), and also because a large horizontal slowness increases the ambiguity of obtaining the vertical slowness from dispersion relations.

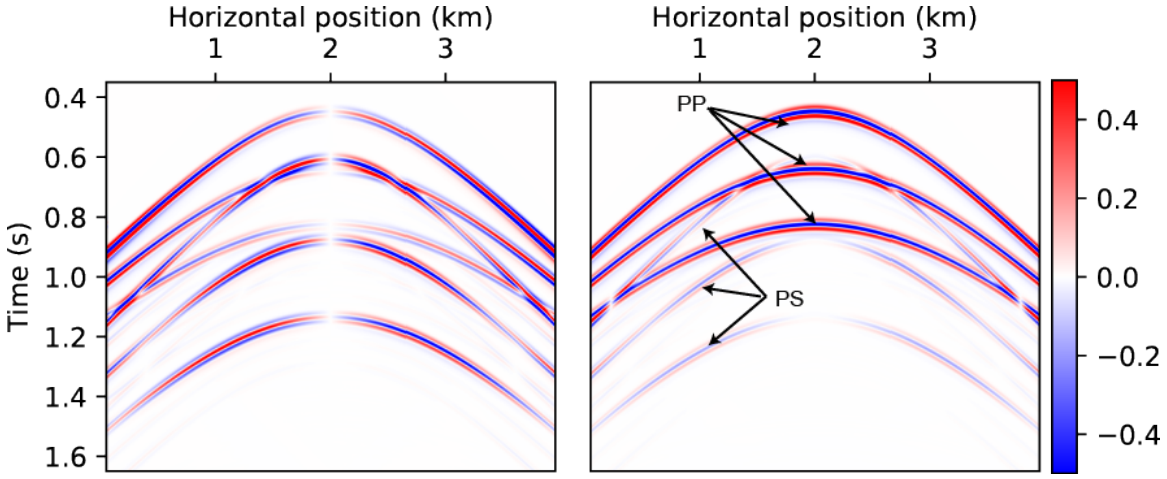

Fig. 2. The horizontal (left) and vertical (right) particle-velocity seismograms, respectively, with the direct waves removed. P- and S-waves coexist in both components.

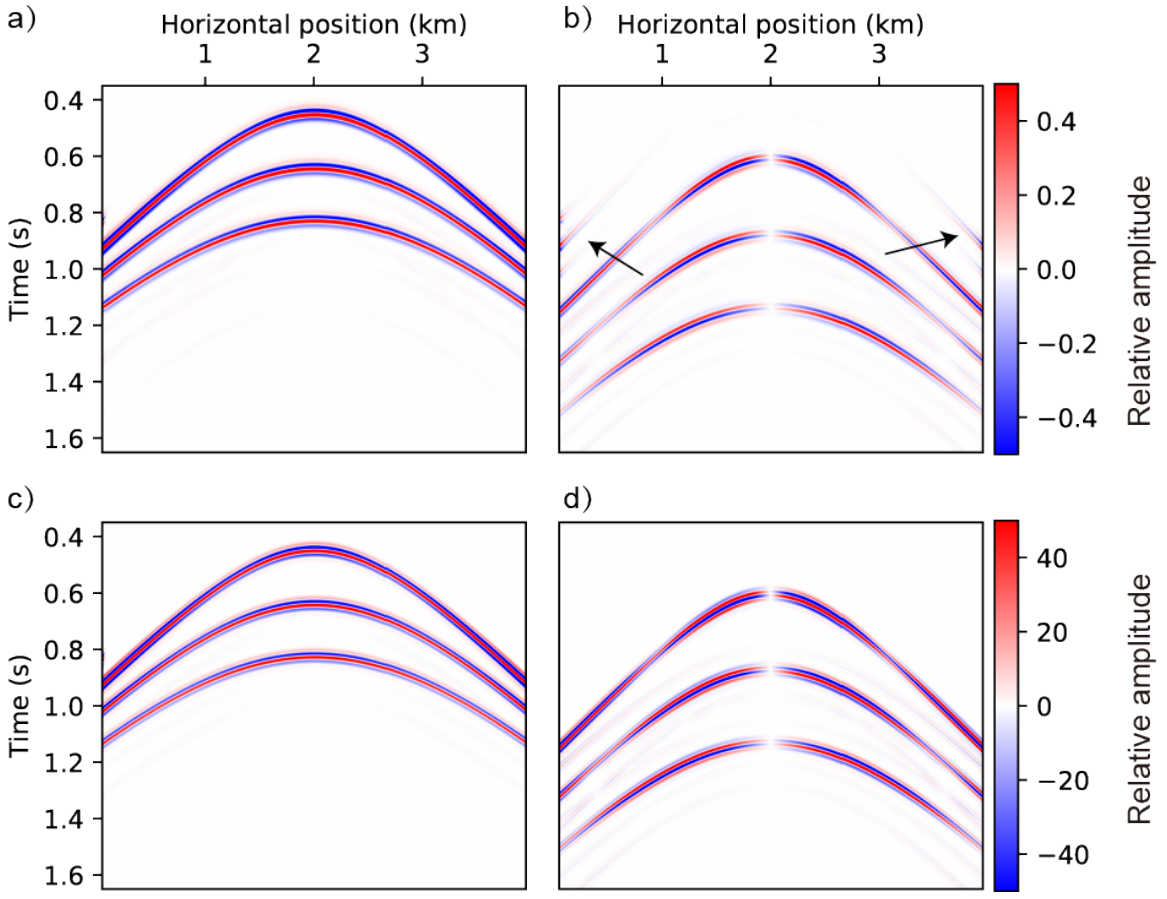

Fig. 3. The (a) and (b) are separated P and S seismograms using the proposed separation algorithm. The decomposition quality decreases at far offsets (black arrows). Compare with P-wave (c) and S-wave (d) seismograms separated with divergence and curl operators during the synthetic forward modeling as benchmarks. Note the relative amplitudes in (a) and (b) are correct as the polarization vectors during PS separation are normalized.

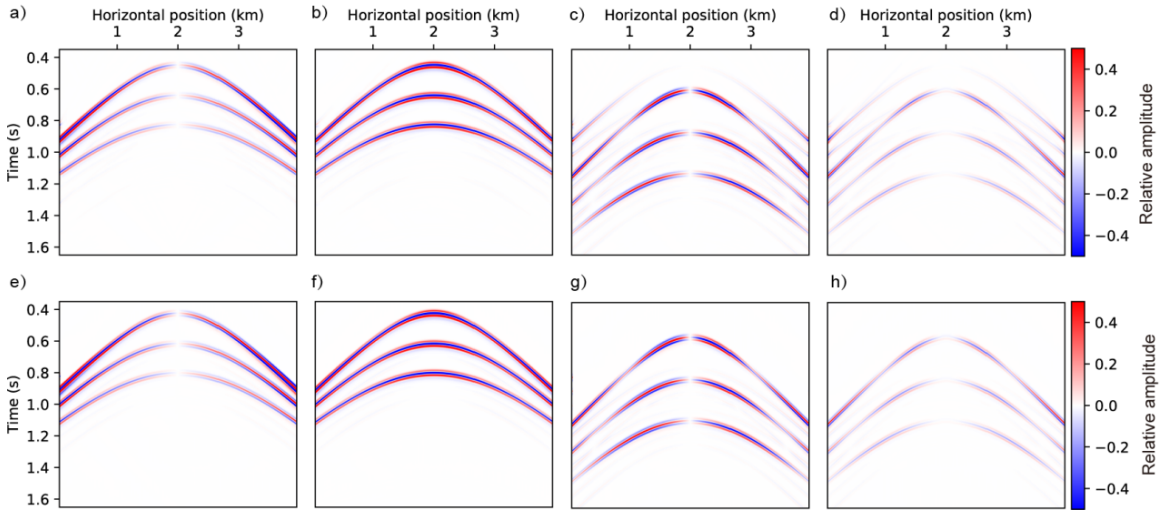

Fig. 4. The (a) horizontal and (b) vertical particle-velocity seismograms of the P-waves obtained with the decomposition algorithm, and the (c) horizontal and (d) vertical particle-velocity seismograms of S-waves obtained by subtracting the P-waves in (a) and (b) from the coupled seismogram in Fig. 2 component-by-component. (e)-(h) are the corresponding decomposition results from the PS decoupled equations.

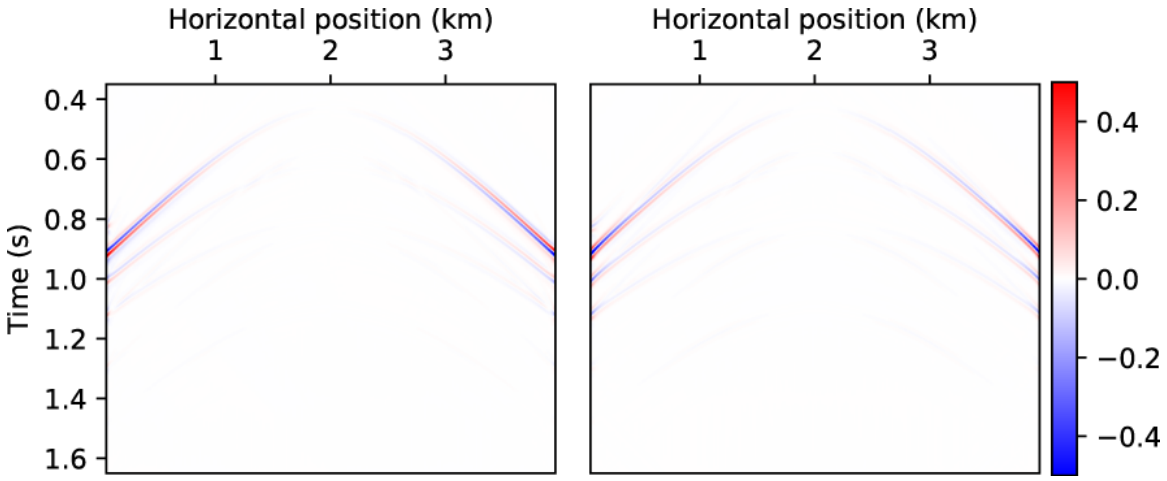

Fig. 5. The horizontal (left) and vertical (right) particle-velocity residuals by subtracting the P-waves in Figs. 4a and 4b from those in Figs. 4e and 4f.

To test the reliability of the P-S separation/decomposition in the presence of noise, we repeat the decomposition test with Gaussian noise added to the input coupled seismograms (Figs. 6a and 6b). The noisy seismograms have a signal to noise ratio (SNR) of -1.4 which means the signal is buried in strong noise. The SNR is calculated as 20log10(S/N), where S and N the L_2 norms of the signal and noise, respectively. The resultant horizontal and vertical P-wave components are in Figs. 6c and 6d, and the corresponding S-waves

are in Figs. 6e and 6f. To evaluate the results, the P-waves decomposed from the noisy data are subtracted from the P-waves decomposed from the clean data; the residuals, in Figs. 6g and 6h, don't have any visible coherent energy, and thus the algorithm is not influenced by this noise level.

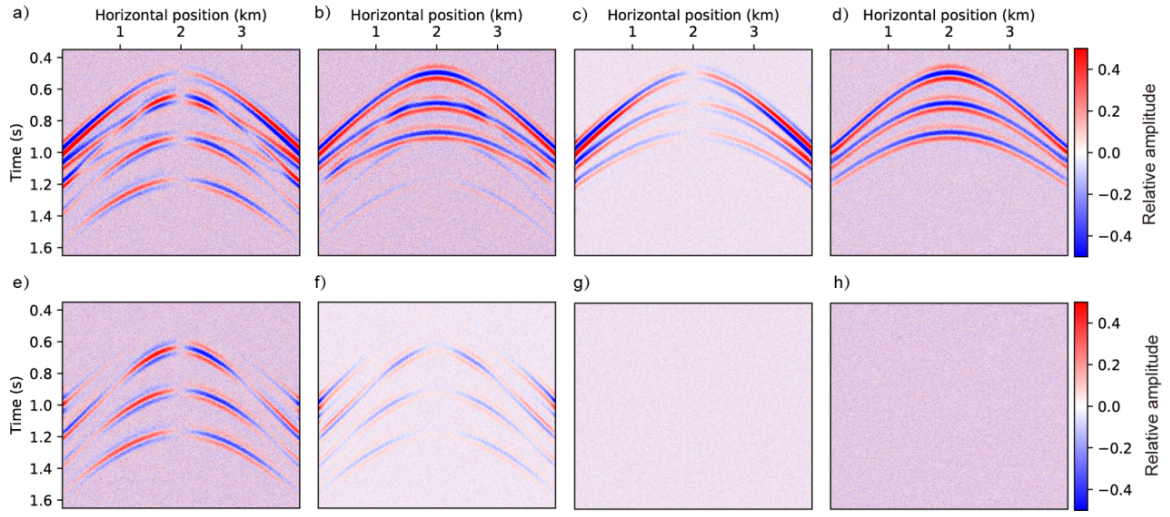

Fig. 6. The (a) horizontal and (b) vertical particle-velocity seismograms with noise. The (c) horizontal and (d) vertical particle-velocity seismograms of the decomposed P-waves, and the (e) horizontal and (f) vertical particle-velocity seismograms of the decomposed S-waves using the decomposition algorithm. (g) and (h) are the residual noise obtained by subtracting the P-waves in (c) and (d), component-by-component, from the P-waves in Figs. 4(a) and 4(b), which is noise-free.

2D flat-layered anisotropic model example

Now, we modify the flat-layered model to include (VTI) anisotropy with the same acquisition geometry. The model parameters for the four layers are V_{P0} = (2.5, 2.6, 2.7, 2.8) km/s, V_{S0} = (1.2, 1.25, 1.3, 1.35) km/s, ρ = (2.1, 2.1, 2.1, 2.1) g/cm^3, ϵ = (0.1, 0.1, 0.2, 0.25), and δ = (0.1, 0.1, 0.1, 0.15, 0.2). The dominant frequency of the Ricker wavelet of the explosive source is 10 Hz.

Fig. 7 shows the corresponding synthetic 'observed' PS coupled seismogram with the direct waves removed. Unlike in the isotropic model, sources in the anisotropic model generate both P- and S-waves, so the recorded reflections include PP, PS, SP and SS waves, but the SP waves are too weak to be seen in this example.

Only the decomposition algorithm is tested in this example. The parameters from the first layer are input to the algorithm. Figs. 8a-d contain the PS decomposition results obtained using the proposed method. To

compare, the benchmark P- and S-waves, which are decomposed during the forward modeling by solving the Christoffel equation (Zhang and McMechan, 2010) at every timestep, are plotted in Figs. 8e-h. Fig. 9 shows the residuals between the decomposed P-waves in Figs. 8a and 8b and the benchmark P-waves in Figs. 8e and 8f. Even with consideration of the anisotropy parameters, the SS reflection cannot be fully decomposed from the coupled waves because of its large horizontal slowness.

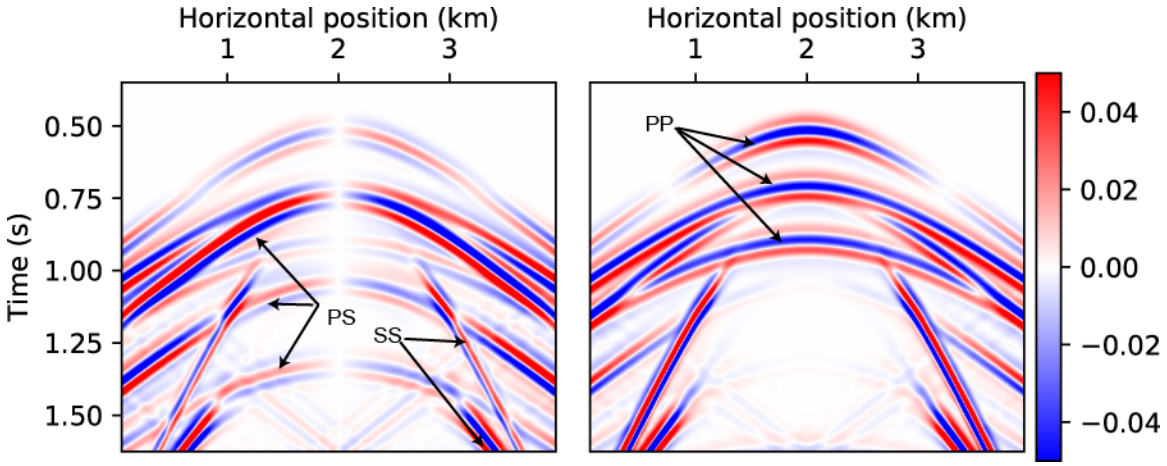

Fig. 7. The horizontal (left) and vertical (right) particle-velocity seismograms that are generated by the anisotropic layered model, with the direct waves removed.

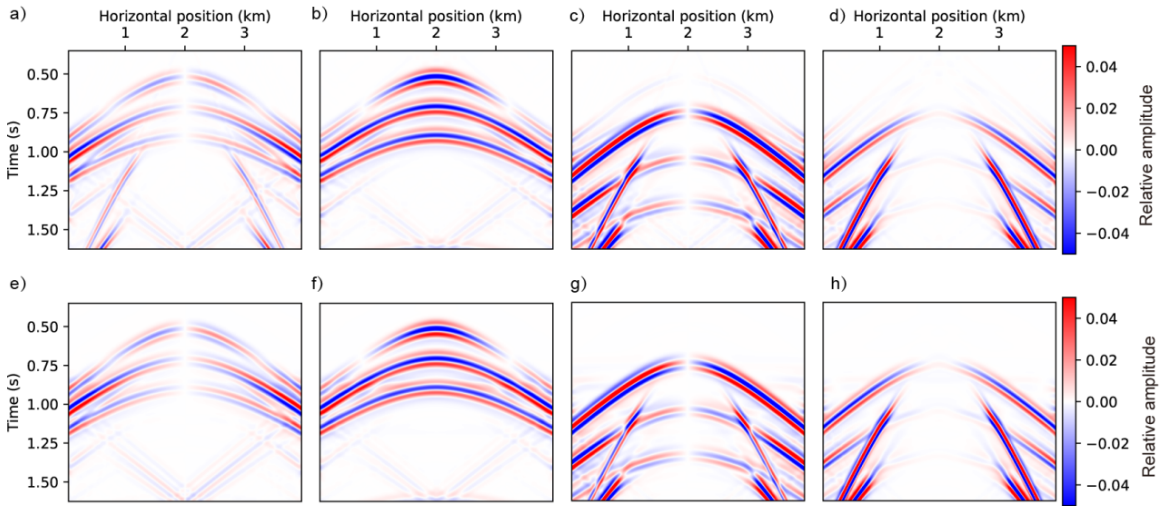

Fig. 8. The (a) horizontal and (b) vertical particle-velocity seismograms of the P-waves obtained with the decomposition algorithm, and the (c) horizontal and (d) vertical particle-velocity seismograms of S-waves obtained by subtracting the P-waves in (a) and (b) from the coupled seismogram in Fig. 7 component-by-component. (e)-(h) are the corresponding decomposition results by solving the Christoffel equation during the forward modeling.

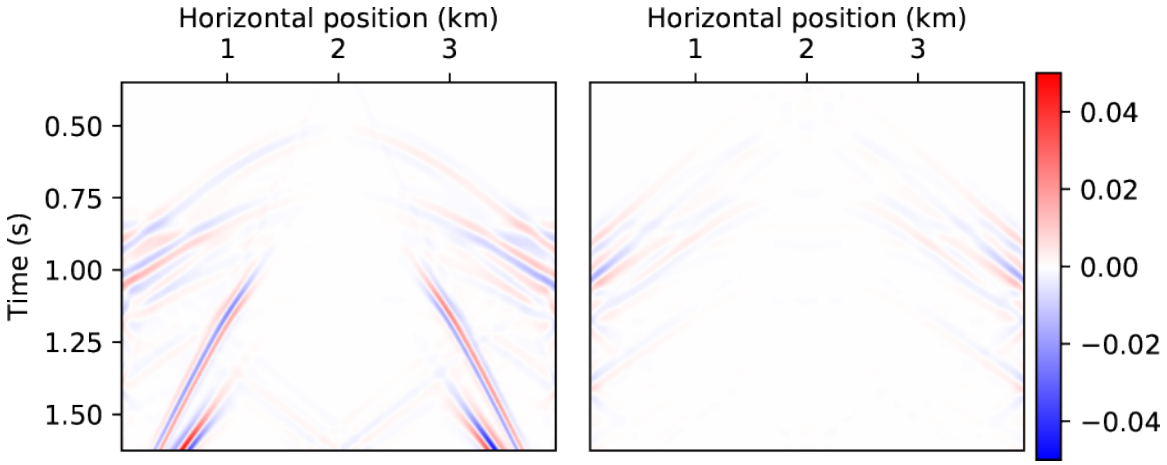

Fig. 9. The horizontal (left) and vertical (right) particle-velocity residuals obtained by subtracting the P-waves in Figs. 8a and 8b from those in Figs. 8e and 8f.

2D Marmousi2 example with a heterogeneous near-surface zone

The next synthetic test is performed on a portion of the elastic Marmousi2 model (Martin et al., 2006). The model (Fig. 10) is isotropic, and it is modified by removing the uppermost water layer. The grid intervals in both x- and z-directions are 5 m, and the time increment is 0.5 ms. An explosive source with a 15-Hz Ricker wavelet is placed at (x, z) = (2.5, 0.025) km. 1001 receivers are located along the model surface with 5 m spacing. The recorded elastic common-source gather is shown in Fig. 11. Figs. 12a and 12b are the separated P- and S-waves using constant surface V_P and V_S. The near-surface velocity zone is then divided into 21 sections as indicated in Figs. 10a and 10b. The P- and S-waves separated with the proposed separation algorithm are in Figs. 12c and 12d, respectively, which has fewer artifacts than those in Figs. 12a and 12b, and are similar to the results obtained using the divergence and curl operators in Figs. 12e and 12f, except that no amplitude corrections are needed in Figs. 12a-d.

Figs. 13a-d contain the decomposed P- and S-waves using the decomposition algorithm, which does not require wavefield extrapolations. For comparison, Figs. 14a-d are the decomposed 2-component P- and S-waves generated with forward modeling using the decoupled equations. Residuals between the decomposed P-waves in Figs. 13a and 13b and those in Figs. 13a and 13b are shown in Fig. 15, and are visible only for first arrivals and a few shallow reflections.

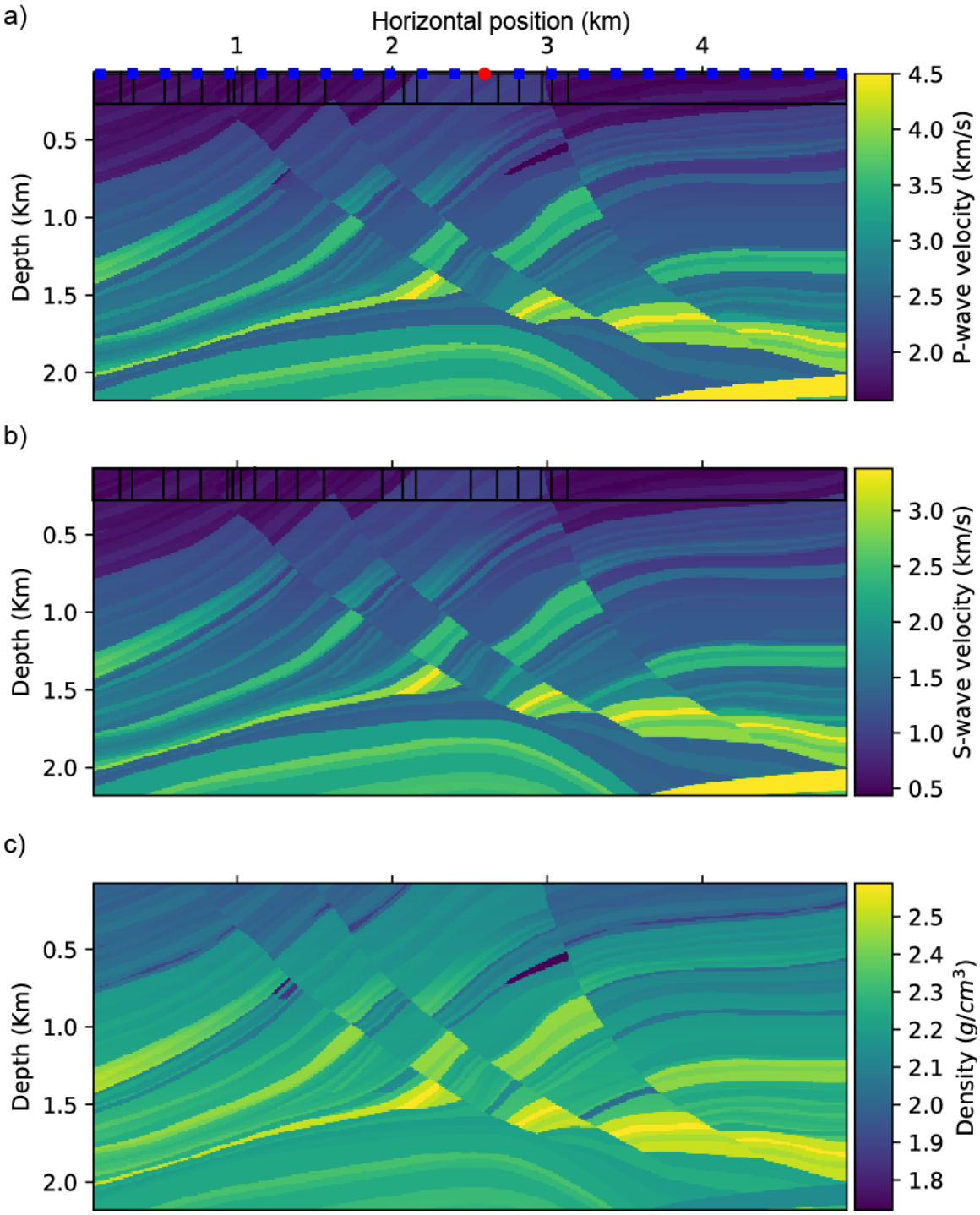

Fig. 10. A portion of the Marmousi2 model. The red dot represents the source location, and the blue squares are every 42nd receiver location. The near-surface velocity zone is divided into 21 sections to implement the proposed separation/decomposition algorithms.

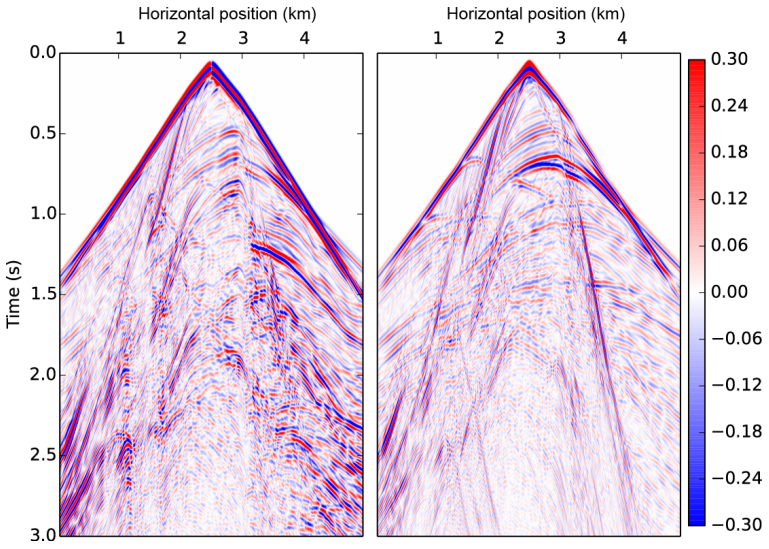

Fig. 11. The horizontal (left) and vertical (right) particle-velocity seismograms from the Marmousi2 model.

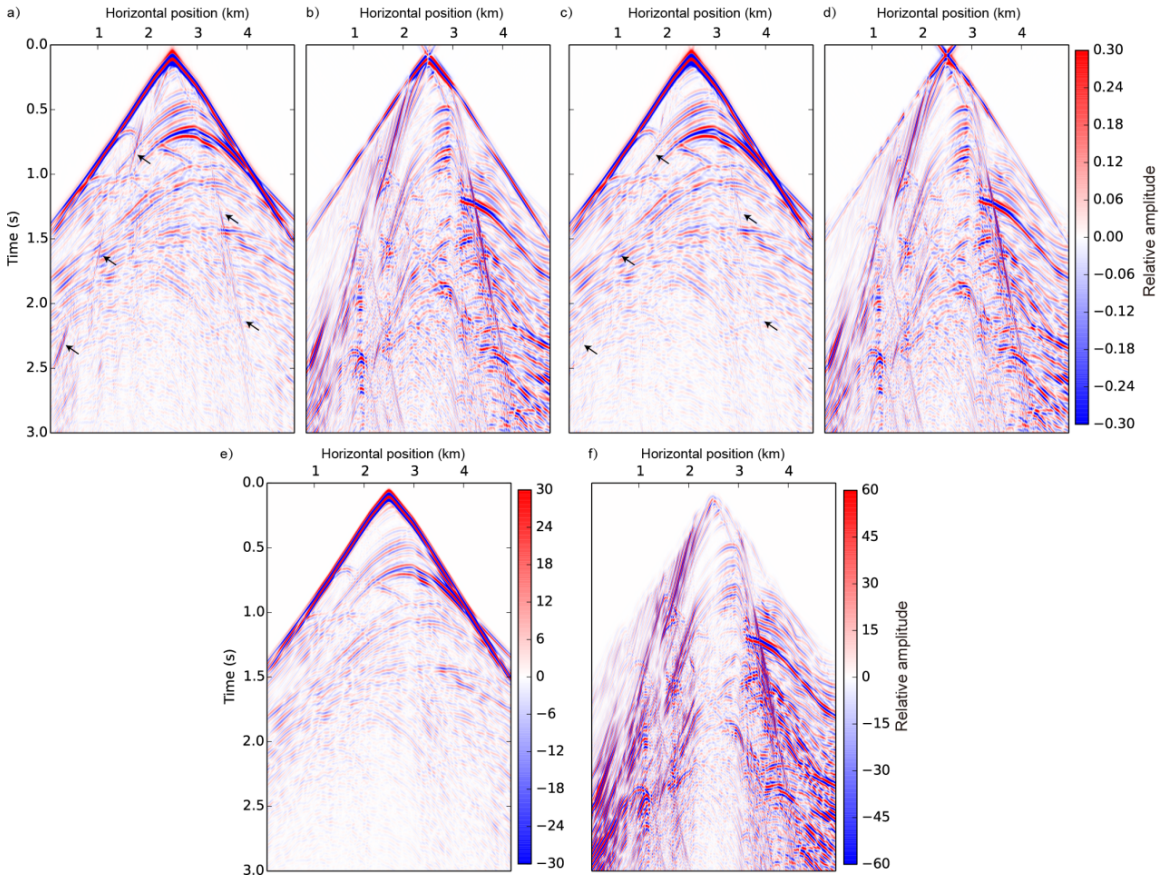

Fig. 12. The (a) P-wave and (b) S-wave seismograms separated using a constant V_P and V_S. (c) and (d) are separated P- and S-wave seismograms with the proposed algorithm using multiple V_P and V_S values by dividing the near-surface velocity zone into 21 sections, and thus give cleaner separation results (indicated by the arrows). Compare with the coupled seismogram in Fig. 11, and with (e) and (f) which are P- and S-wave seismograms generated with divergence and curl operators during the synthetic forward modeling.

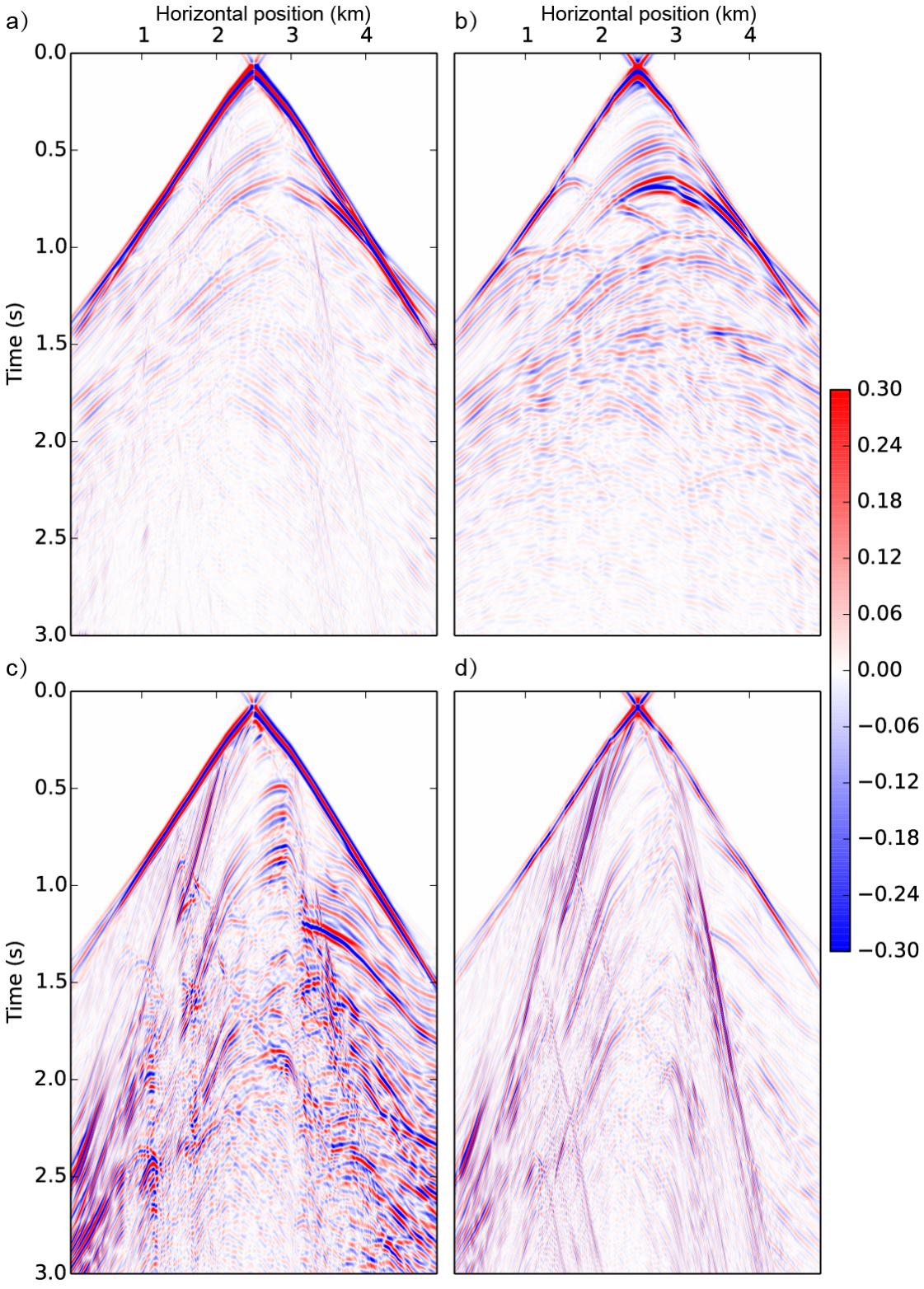

Fig. 13. The (a) horizontal and (b) vertical particle-velocity seismograms of the P-waves obtained with the decomposition algorithm, and the (c) horizontal and (d) vertical particle-velocity seismograms of the S-waves obtained by subtracting the P-waves in (a) and (b) from the coupled particle-velocity seismograms in Fig. 11.

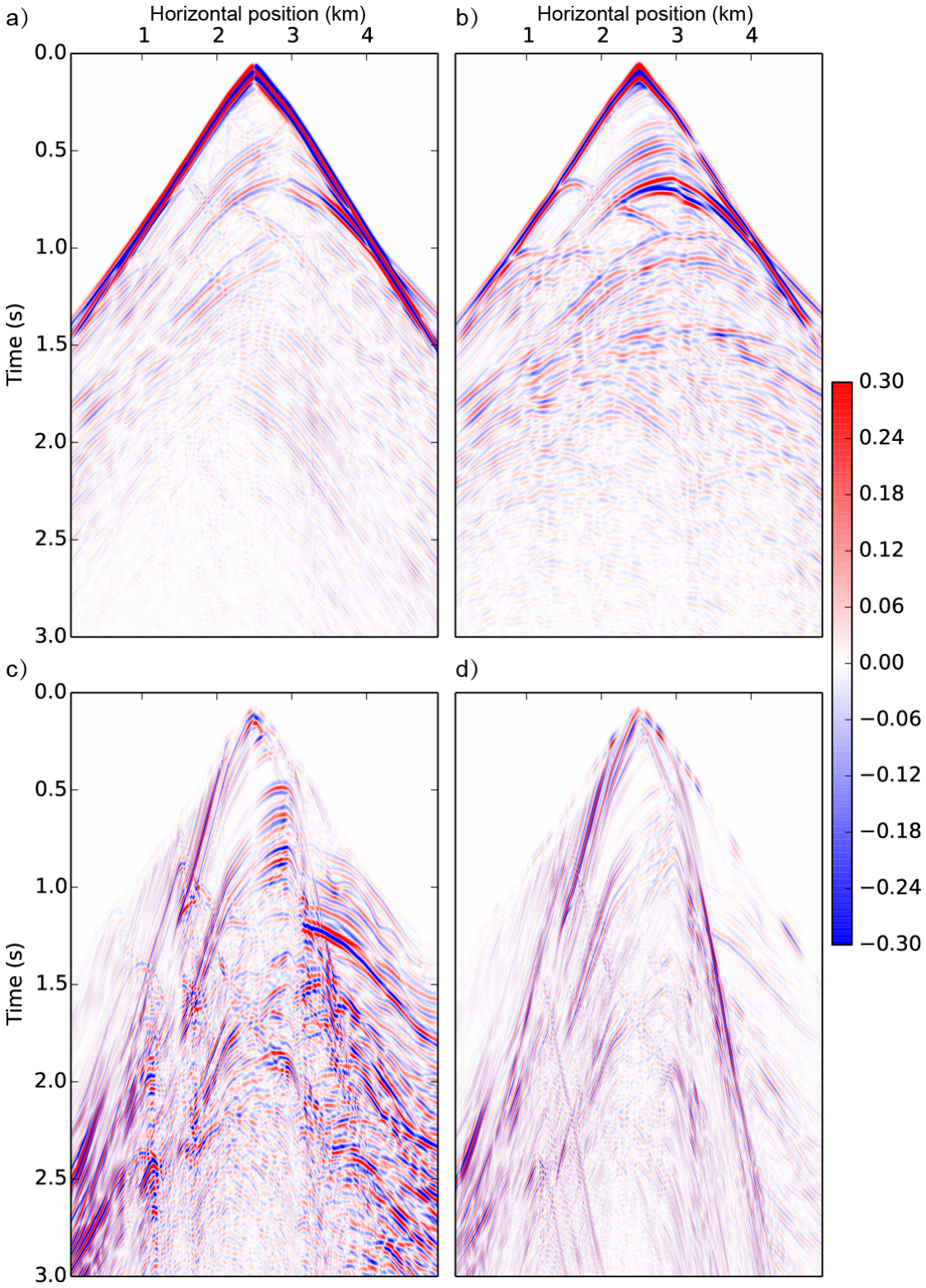

Fig. 14. The (a) horizontal and (b) vertical particle-velocity seismograms of the P-waves generated by modeling with the PS decoupled equations, and the (c) horizontal and (d) vertical particle-velocity seismograms of the S-waves obtained by subtracting the P-waves in (a) and (b) from the coupled particle-velocity seismograms in Fig. 11.

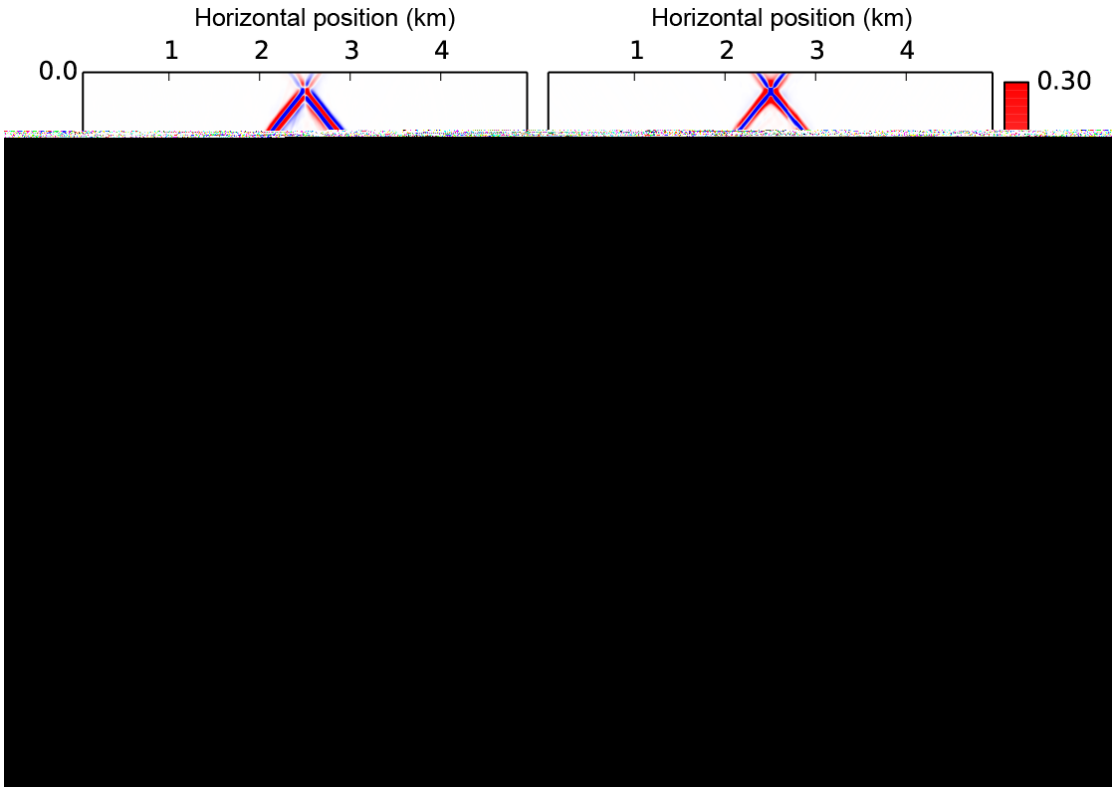

Fig. 15. The horizontal (left) and vertical (right) particle-velocity residuals obtained by subtracting the P-waves in Figs. 14a and 14b from those in Figs. 13a and 13b.

3-D isotropic elastic overthrust model example

The fourth test is performed on a portion of the SEG/EAGE 3D overthrust model (http://geodus1.ta.tudelft.nl/seage3dm/). The S-wave velocity V_S is approximated by dividing the P-wave velocity V_P by 2 at each grid point. The density is set to be a constant of 2.4 g/cm^3. Fig. 16 shows three orthogonal slices through the V_P volume. The spatial sample interval of the model is dx = dy = dz = 25 m. An explosive source with a 15-Hz Ricker wavelet is placed at (x, y, z) = (1.86, 1.86, 0.025) km. 151 x 151 receivers are evenly placed over the surface with a spacing of 25 m. The recorded x, y, and z particle-velocity components on representative orthogonal slices are plotted in Figs. 17a, b, and c, respectively, with the direct waves removed.

The PS decomposition results are analyzed first. Figs. 18a-f are the x, y, and z particle-velocity components of the P- and S-waves calculated with the decomposition algorithm. Figs. 18g-l are the x, y, and z particle-velocity components of the P- and S-waves obtained with the decoupled equations. As explained above, the S-waves are extracted by subtracting the P-waves from the coupled wavefield.

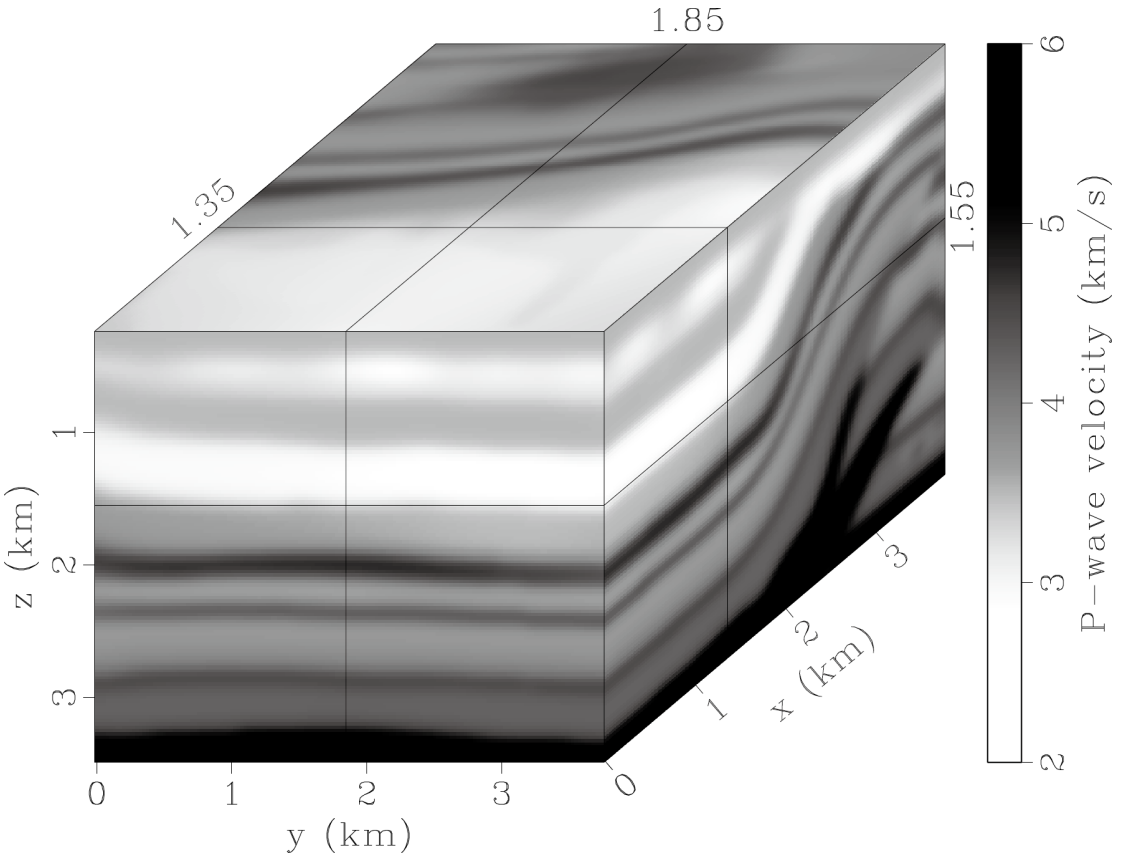

Fig. 16. A portion of the P-wave velocity of the overthrust model.

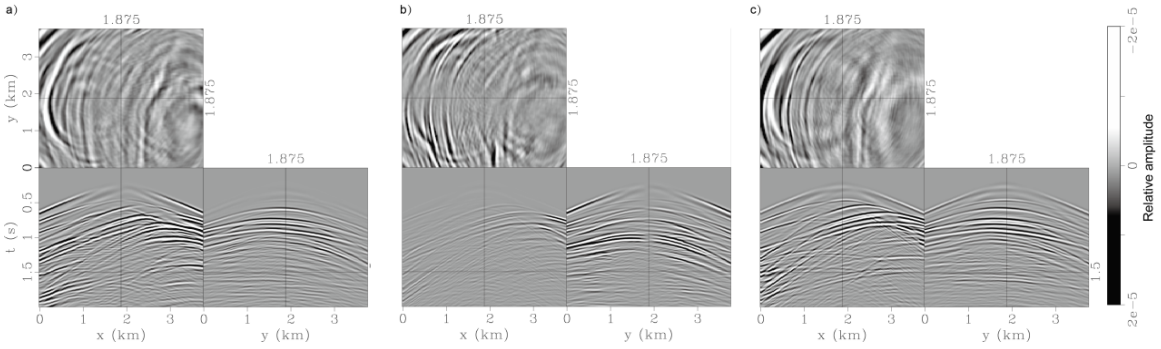

Fig. 17. The (a) x, (b) y and (c) z particle-velocity components of the coupled seismogram from the overthrust model in Fig. 16.

For the PS separation results, only the separated P-waves are analyzed for simplicity. The separated P-waves obtained with the separation algorithm are shown in Fig. 19a. Compare with the P-waves obtained by applying a divergence operator during the forward modeling (Fig. 19b). The two seismograms look similar despite the amplitude differences. Both the separation and decomposition algorithms give similar results compared with their corresponding benchmarks.

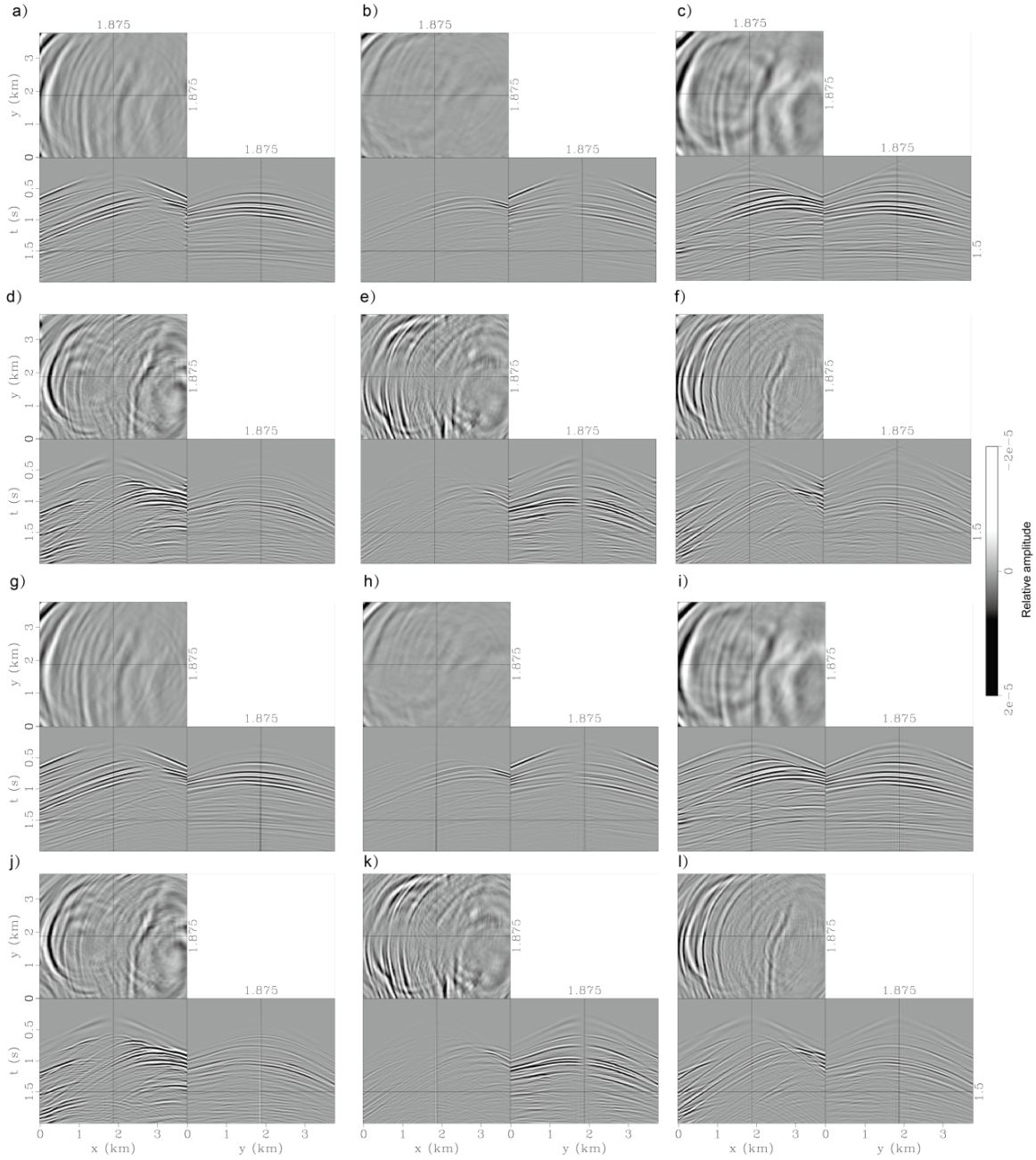

Fig. 18. The (a-c) and (d-f) panels are the corresponding x, y, and z particle-velocity components of the P- and S-wave seismograms, respectively, obtained with the decomposition algorithm. Compare with (g-i) and (j-l) which are the corresponding P- and S-wave particle-velocity components, respectively, with the decoupled equations.

DISCUSSION

The separation and decomposition algorithms are derived from the dispersion relations of isotropic and anisotropic elastic wave equations. The near-surface zone can be homogeneous or heterogeneous. Increased complexity (e.g., viscoelasticity) in the deeper parts of the model does not influence the application of the separation/decomposition algorithms.

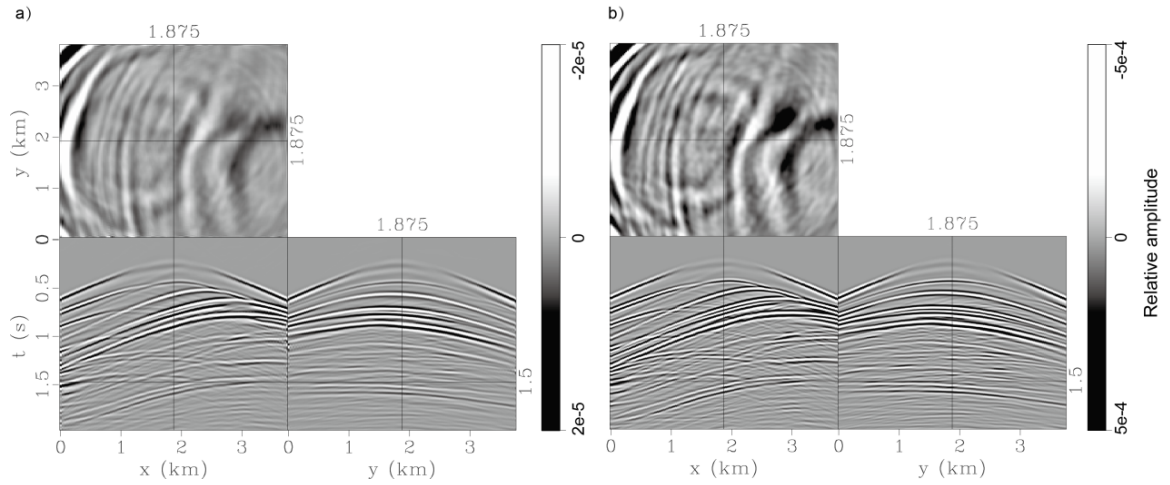

Fig. 19. The separated P-waves from (a) the separation algorithm, and (b) the divergence operators. Notice the amplitude differences in (b) compared to those in (a) and in Fig. 18.

The PS separation algorithm generates single-component P-waves, which is similar to acoustic waves (pressure), so it can be used as input to acoustic-based algorithms. However, the PS separation results are usually distorted in both phase and amplitude. The PS decomposition results are free from distortion by preserving all component information. The generated P- and S-waves both have multi-components, and can be input to elastic RTMs or full-wave inversions.

One limitation of the algorithms is that all recorded waves are assumed to be up-going waves, so the signs of k_z in the dispersion relations can be defined. Multi-component seismograms obtained from the seafloor can be separated into up-going and down-going waves (White, 1965) before applying the PS separation/decomposition algorithms discussed above. In 3D, the S-waves can be further separated into SV- and SH-modes, but this cannot be achieved by the proposed method alone, as they share the same S-wave velocity; analysis of shear-wave polarizations and splitting caused by anisotropy could be achieved using an anisotropic propagator to produce the data and the Christoffel equation, but this is beyond the scope of the present paper.

The accuracy of PS separation/decomposition decreases as offset increases. The large horizontal slowness at far offsets reduces the accuracy in calculating the vertical slowness from dispersion relations. Thus caution is needed when processing large offset data using this algorithm. The separated/decomposed P- and S-seismograms can potentially be used as input to tomography, velocity analysis, reverse-time migration and full-wave inversions.

CONCLUSIONS

We analyze a pair of algorithms that can perform both P- and S-wave separation and vector decomposition of multi-component common-source gathers in both isotropic and anisotropic media. The algorithms are extended to 3D, and are efficient as no elastic extrapolations are required. Because the method is derived from the P- and S-wave dispersion relations, near-surface model parameters need to be provided, and near-surface heterogeneity can be properly handled by processing in sections. No knowledge of the deeper velocities is required, and there are no assumptions about the origin of the recorded P- and S-waves. By comparing with benchmarks, it is demonstrated that the separated P- and S-waves obtained using this method do not have amplitude-distortion problems as with divergence and curl operators, but the phase still needs to be corrected. Tests with synthetic data from 2D and 3D models show high-accuracy separation and decomposition.

ACKNOWLEDGEMENTS

The research leading to this paper is supported by the National Natural Science Foundation of China under grant number NSFC 41804108, by the Fundamental Research Funds for the Central Universities under grant number 01113026, and by the Sponsors of the UT-Dallas Geophysical Consortium. A portion of the computations were done at the Texas Advanced Computing Center. This paper is Contribution No. 1347 from the Department of Geosciences at the University of Texas at Dallas.

REFERENCES

Amundsen, L., 1995. Decomposition of multicomponent sea-floor data into upgoing and downgoing P- and S-waves. Geophysics, 60: 563-572.

Dankbaar, J.W.M., 1985. Separation of P- and S-waves. Geophys. Prosp., 33: 970-986.

Dellinger, J. and Etgen, J., 1990. Wave-field separation in two-dimensional anisotropic media. Geophysics, 55: 914-919.

Devaney, A.J. and Oristaglio, M.L., 1986. A plane-wave decomposition for elastic wavefields applied to the separation of P-waves and S-waves in vector seismic data. Geophysics, 51: 419-423.

Greenhalgh, S.A., Mason, I.M., Lucas, E., Pant, D. and Eames, R.T., 1990. Controlled direction reception filtering of P- and S-waves in τ-p space. Geophys. J. Internat., 100: 221-234.

Komatitsch, D. and Martin, R., 2007. An unsplit convolutional perfectly matched layer improved at grazing incidence for the seismic wave equation. Geophysics, 72(5): SM155-SM167.

Li, Z., Gu, B., Ma, X. and Liang, G., 2015. Separating P- and S-waves in prestack elastic seismograms using the equivalent form of the elastic wave equation. J. Appl. Geophys., 114: 210-223.

Li, Z., Ma, X., Fu, C., Gu, B. and Liang, G., 2016. Frequency-wavenumber implementation for P- and S-wave separation from multi-component seismic data. Explor. Geophys., 47: 32-43.

Ma, D. and Zhu, G., 2003. P- and S-wave separated elastic wave equation numerical modeling (in Chinese). Oil Geophys. Prosp. 38: 482-486.

Martin, G.S., Wiley, R. and Marfurt, K.J., 2006. Marmousi2: An elastic upgrade for Marmousi. The Leading Edge, 25: 156-166.

Morse, P.M. and Feshbach, H., 1953. Methods of Theoretical Physics. McGraw-Hill Book Company, New York.

Pedersen, Ø., Ursin, B. and Stovas, A., 2007. Wide-angle phase-slowness approximations in VTI media. Geophysics, 72(4): S177-S185.

Schoenberg, M.A. and de Hoop, M.V., 2000. Approximate dispersion relations for qP-qSV-waves in transversely isotropic media. Geophysics, 65: 919-933.

Stanton, A. and Sacchi, M.D., 2017. Elastic least-squares one-way wave-equation migration. Geophysics, 82(4): S293-S305.

Sun, R., 1999. Separating P- and S-waves in a prestack 2-dimensional elastic seismogram. Extended Abstr., 61st EAGE Conf., Helsinki: 6-23.

Sun, R., Chow, J. and Chen, K.J., 2001. Phase correction in separating P- and S-waves in elastic data. Geophysics, 66: 1515-1518.

Thomsen, L., 1986. Weak elastic anisotropy. Geophysics, 51: 1954-1966.

van der Baan, M., 2006. PP/PS wavefield separation by independent component analysis. Geophys. J. Internat., 166: 339-348.

Virieux, J., 1986. P-SV wave propagation in heterogeneous media: Velocity-stress inite-difference method. Geophysics, 51: 889-901.

Wang, C. and Cheng, J., 2017. P/S separation of multi-component seismogram recorded in anisotropic media. Extended Abstr., 79th EAGE Conf., Paris: Tu P3 04.

Wang, W. and McMechan, G.A., 2015. Vector-based elastic reverse-time migration. Geophysics, 80(6): S245-S258.

Wang, W., McMechan, G.A., Tang, C. and Xie, F., 2016. Up/down and P/S decompositions of elastic wavefields using complex seismic traces with applications to calculating Poynting vectors and angle-domain common-image gathers from reverse time migrations. Geophysics, 81(4): S181-S194.

Wang, W., McMechan, G.A. and Zhang, Q., 2015. Comparison of two algorithms for isotropic elastic P- and S-vector decomposition. Geophysics, 80(4): T147-T160.

Wang, Y., Singh, S. and Barton, P.J., 2002. Separation of P- and SV-wavefields from multicomponent seismic data in the τ-p domain. Geophys. J. Internat., 151: 663-672.

Wapenaar, C.P.A., Herrmann, P., Verschuur, D.J. and Berkhout, A.J., 1990. Decomposition of multicomponent seismic data into primary P- and S-wave responses. Geophys. Prosp., 38: 633-661.

White, J.E., 1965. Seismic Waves: Radiation, Transmission and Attenuation. McGraw-Hill Book Company, New York.

Xiao, X. and Leaney, W.S., 2010. Local vertical seismic profiling (VSP) elastic reverse-time migration and migration resolution: Salt-flank imaging with transmitted P-to-S waves. Geophysics, 75(2): S35-S49.

Yao, D., Zhou, X. and Zhong, B., 1993. Method for separating out P-wave or S-wave in VSP data and its application. Oil Geophys. Prosp., 28: 623-628.

Zhang, J., Tian, Z. and Wang, C., 2007. P- and S-wave separated elastic wave equation numerical modeling using 2D staggered-grid. Expanded Abstr., 77th Ann. Internat. SEG Mtg., San Antonio: 2104-2109.

Zhang, Q. and McMechan, G.A., 2010. 2D and 3D elastic wavefield vector decomposition in the wavenumber domain for VTI media. Geophysics, 75(3): D13-D26.

Zhu, H., 2017. Elastic wavefield separation based on the Helmholtz decomposition. Geophysics, 82(2): S173-S183.

Zhu, X., Altan, S. and Li, J., 1999. Recent advances in multicomponent processing. The Leading Edge, 18: 1283-1288.